

Hydrodynamical simulations of the Sunyaev–Zel'dovich effect: cluster scaling relations and X-ray properties

Antonio C. da Silva,^{1,2*} Scott T. Kay,³ Andrew R. Liddle³ and Peter A. Thomas³

¹*IAS, Bâtiment 121, Université Paris Sud, F-91405, Orsay, France*

²*Observatoire Midi-Pyrénées, Av. Edouard Belin 14, 31500 Toulouse, France*

³*Astronomy Centre, University of Sussex, Falmer, Brighton BN1 9QJ*

20 March 2019

ABSTRACT

The Sunyaev–Zel'dovich effect is a powerful new tool for finding and studying clusters at high redshift, particularly in combination with their X-ray properties. In this paper we quantify the expected scaling relations between these properties using numerical simulations with various models for heating and cooling of the cluster gas. For a *Non-radiative* model, we find scaling relations in good agreement with self-similar predictions: $Y \propto T_X^{5/2}$ and $Y \propto L_X^{5/4}$. Our main results focus on predictions from *Cooling* and *Preheating* simulations, shown by Muanwong et al. (2002) to provide a good match to the X-ray scaling relations at $z = 0$. For these runs we find slopes of approximately $Y \propto T_X^3$ and $Y \propto L_X$, steeper and flatter than the self-similar scalings respectively. We also study the redshift evolution of the scaling relations and find the slopes show no evidence of evolution out to redshifts well beyond one, while the normalizations of relations between the SZ signal and X-ray properties do show evolution relative to that expected from self-similarity, particularly at $z < 1$.

Key words: hydrodynamics - methods: numerical - X-rays: galaxies: clusters - cosmic microwave background

1 INTRODUCTION

The prospect of surveying for galaxy clusters across a wide range of redshifts using the Sunyaev–Zel'dovich (SZ) effect (Sunyaev & Zel'dovich 1972, 1980) raises the hope of a much-improved understanding of cluster physics, and in particular of the evolution of the cluster gas. The SZ effect is a particularly powerful tool when combined with observations of X-ray emission from the hot cluster gas, as the two techniques probe different properties of the cluster gas distribution, and with the *XMM-Newton* and *Chandra* X-ray satellites in their main operations phases the number of clusters and groups with quality X-ray observations is rapidly increasing. It is therefore timely to extend theoretical models of clusters, where efforts have hitherto been concentrated upon their X-ray properties, to incorporate predictions for the SZ effect.

Numerical simulations indicate that the distribution of non-baryonic dark matter in clusters, which dominates their mass, is approximately self-similar (e.g. Navarro, Frenk & White 1995, 1997). Observations indicate, however, that the baryonic gas component cannot share such a degree of self-

similarity. This is particularly evident from observations of the L_X-T_X relation, which show it to be steeper than predicted by the self-similar model (e.g. Edge & Stewart 1991; Xue & Wu 2000). The reason for this discrepancy is that the gas is less centrally concentrated than the dark matter, due to physical processes (in addition to gravity) that raised the entropy of the gas (e.g. Evrard & Henry 1991; Kaiser 1991; Bower 1997; Voit et al. 2002; Ponman, Sanderson & Finoguenov 2003). This entropy could come from direct heating of the hot gas from stars or AGN (e.g. Wu, Fabian & Nulsen 2000; Bower et al. 2001; Quilis, Bower & Balogh 2001), or from radiative cooling which transforms low-entropy material into stars allowing high-entropy material to flow in to replace it (e.g. Knight & Ponman 1997; Pearce et al. 2000; Bryan 2000). Understanding the relative importance of heating and cooling, and how these processes conspire to establish excess entropy in clusters, is one of the key problems in cluster gas physics.

The implications of an excess of entropy on the global properties of the SZ effect (e.g. source counts, the mean Compton parameter and the angular power spectrum) has previously been investigated using both analytical techniques (e.g. Cavaliere & Menci 2001; Holder & Carlstrom 2001; Zhang & Wu 2003) and numerical simulations (e.g.

* E-mail:antonio.dasilva@ias.u-psud.fr

Springel, White & Hernquist 2001; da Silva et al. 2001; White, Hernquist & Springel 2002). The mass dependence of the SZ effect in clusters has been addressed by Metzler (1998) and by White et al. (2002). More recently, McCarthy et al. (2003a) used a semi-analytic model to derive scaling relations between the central Compton parameter and mass, temperature, SZ flux density and X-ray luminosity. These scalings were subsequently used in a companion paper (McCarthy et al. 2003b) to estimate the level of the entropy floor compatible with present-day SZ observations.

The purpose of this paper is to investigate the relationship between SZ and X-ray properties of clusters in N -body/hydrodynamical simulations that include models for both cooling and preheating. The simulations we use have already been demonstrated to give good overall agreement with observed X-ray scaling relations at redshift zero (Muanwong et al. 2001; Thomas et al. 2002; Muanwong et al. 2002). Our approach is mainly focused on the derivation of theoretical scaling laws, and their evolution with redshift, between the integrated SZ flux density and other cluster properties, such as X-ray temperature and luminosity. We quantify deviations from self-similar evolution on both the slope and normalization of the scalings and provide fits which can be used for comparison with other theoretical models and observations. An observationally-motivated analysis of SZ/X-ray correlations, that can be more readily applied to ‘blind’ searches for high-redshift clusters, will be presented in a future paper.

This paper is organized as follows. We define the observational quantities used and the simple scaling laws predicted by the self-similar model in Section 2. Details of our simulations and how our cluster catalogues were constructed are presented in Section 3. In Section 4, we investigate the correlation between thermal SZ integrated flux and other 3D cluster properties (mass, mass-weighted and emission-weighted temperature and X-ray luminosity) from the simulation data at redshift zero. The evolution of these relations with redshift is studied in Section 5, before we draw conclusions in Section 6.

2 THEORETICAL FRAMEWORK

2.1 Definitions of physical quantities

The SZ effect arises due to inverse Compton scattering of CMB photons off free electrons, with the largest SZ signal being produced by intracluster gas. The total SZ flux density produced by a cluster is the integral of the SZ sky brightness over its subtended solid angle

$$S_\nu = I_0 \int [g(x) y - h(x) b] d\Omega, \quad (1)$$

where $I_0 = 2(k_B T_0)^3 / (hc)^2 \simeq 2.28 \times 10^4$ mJy arcmin $^{-2}$,¹ for a mean CMB temperature of $T_0 \simeq 2.725$ K (Mather et al. 1999). The first term inside the brackets accounts for the thermal SZ effect, due to internal motion of the electrons, whereas the second term, the kinetic SZ effect, is the contribution due to bulk motion of the gas. We ignore the kinetic

¹ 1 mJy = 10^{-26} erg s $^{-1}$ m $^{-2}$ Hz $^{-1}$.

SZ effect in this paper as the thermal SZ effect dominates at all frequencies except $\nu \simeq 217$ GHz ($x = h\nu/k_B T_0 \simeq 3.83$).

The Comptonization parameter y contains information on the structure of the intracluster gas

$$y = \frac{k_B \sigma_T}{m_e c^2} \int T_e n_e dl, \quad (2)$$

where T_e and n_e are the temperature and density of the electrons, $\sigma_T \simeq 6.65 \times 10^{-25}$ cm 2 the Thomson cross-section, c the speed of light and m_e the electron rest mass. It is therefore convenient to define the integrated contribution to S_ν from y

$$Y = \int y d\Omega = \int \frac{y}{d_A^2} dA = \frac{k_B \sigma_T}{m_e c^2 d_A^2} \int_V T_e n_e dV, \quad (3)$$

where d_A is the angular diameter distance to the cluster. Since Y depends on distance, we will usually work with the intrinsic thermal SZ signal, defined as $Y^{\text{int}} = Y d_A^2(z)$.

The X-ray luminosity of a cluster is

$$L_X = \int n_e n_H \Lambda_c(T) dV. \quad (4)$$

The integral is over the volume of the cluster and $\Lambda_c(T)$ denotes the cooling rate of the gas, assuming collisional ionization equilibrium. At temperatures above a few keV, the emission is dominated by thermal bremsstrahlung, but below this line emission becomes important.

2.2 Self-similar scaling relations

In the absence of any non-gravitational heating and cooling processes, clusters scale self-similarly to a good approximation (Kaiser 1986; Navarro et al. 1995). In self-similar models, the temperature of the gas scales with the cluster mass as

$$T \propto M^{2/3}(1+z), \quad (5)$$

assuming the density of the gas scales with the mean density $\rho \propto (1+z)^3$ and the system is in virial equilibrium. Applying this to Eq. (3) we get

$$Y^{\text{int}} \propto \begin{cases} f_{\text{gas}} T^{5/2} (1+z)^{-3/2} \\ f_{\text{gas}} M^{5/3} (1+z), \end{cases} \quad (6)$$

where f_{gas} is the gas mass fraction of the cluster.

The X-ray luminosity of a self-similar cluster scales as

$$L_X \propto \begin{cases} f_{\text{gas}}^2 T^2 (1+z)^{3/2} \\ f_{\text{gas}}^2 M^{4/3} (1+z)^{7/2}, \end{cases} \quad (7)$$

assuming that the X-rays are due to bremsstrahlung emission ($\Lambda_c \propto T^{1/2}$).

3 METHOD

3.1 Simulation details

Results are presented from three simulations, described in detail elsewhere (Thomas et al. 2002; Muanwong et al. 2002); we summarize pertinent details here.

We assume a Λ CDM cosmology, setting the density parameter, $\Omega_m = 0.35$, cosmological constant, $\Omega_\Lambda = 0.65$, hubble parameter, $h = 0.71$, baryon density, $\Omega_b h^2 = 0.019$, CDM power spectrum shape parameter, $\Gamma = 0.21$, and

normalization $\sigma_8 = 0.9$. These values are similar to those favoured by current observations including *WMAP*. Initial conditions were generated using 160^3 particles each of baryonic and dark matter, perturbed from a regular grid of comoving length, $L = 100h^{-1}\text{Mpc}$. These choices set the gas and dark matter particle masses equal to $2.6 \times 10^9 h^{-1}\text{M}_\odot$ and $2.1 \times 10^{10} h^{-1}\text{M}_\odot$ respectively.

The runs were started at redshift $z = 49$ and evolved to $z = 0$ using a parallel version of the HYDRA *N*-body/hydrodynamics code (Couchman, Thomas & Pearce 1995; Pearce & Couchman 1997; Thacker & Couchman 2000). The gravitational softening was fixed at $50h^{-1}\text{kpc}$ in comoving co-ordinates until $z = 1$, then at $25h^{-1}\text{kpc}$ in physical co-ordinates until $z = 0$.

The simulations differed only in the adopted heating/cooling model. In the first model, a *Non-radiative* simulation, the gas was subject only to gravitational, adiabatic and viscous forces, and so could only change its entropy through shock-heating. This model fails to reproduce the X-ray scaling relations (Muanwong et al. 2001) but nevertheless can be used to test the self-similar scalings presented in the previous section.

The second simulation, a *Cooling* model, allowed gas to cool radiatively as described by Thomas & Couchman (1992). Tabulated values of Λ_c were generated from cooling tables in Sutherland & Dopita (1993), assuming a time-varying global gas metallicity, $Z = 0.3(t/t_0)Z_\odot$, where $t_0 \simeq 12.8$ Gyr is the current age of the Universe. To increase run-time efficiency, cooled material (all gas particles with temperatures $T < 1.2 \times 10^4$ K and overdensities $\delta > 1000$) was converted into collisionless particles. The global fraction of cooled gas in the simulation box is ~ 15 per cent at $z = 0$. The removal of this gas from the hot phase sufficiently increases the entropy in the centres of clusters to reproduce the X-ray scaling relations, but the cooled fraction is 2 to 3 times higher than observed (Cole et al. 2001). In this respect, this run provides a maximum variation of Y from a cluster due to effect of radiative cooling alone.

Finally, the third simulation, a *Preheating* model, also allowed the gas to cool radiatively, but the gas was impulsively heated by 1.5 keV per particle at $z = 4$. This generates the required minimum entropy in the centres of clusters but prevents further cooling to 10^4 K; the global fraction of cooled gas in the simulation box is only ~ 0.5 per cent at $z = 0$.

3.2 Cluster selection and SZ/X-ray estimators

Clusters were selected by first creating a minimal-spanning tree of all dark matter particles whose density exceeds $\delta = 178\Omega^{-0.55}(z)$ times the mean dark matter density (the approximate value for a virialized sphere, as predicted by the spherical top-hat model; Eke, Navarro & Frenk 1998). The tree was then pruned into clumps using a maximum linking length equal to $0.5\delta^{-1/3}$ times the mean interparticle separation. A sphere was then grown around the densest particle in each clump until the enclosed mean density exceeded a value Δ in units of the comoving critical density. For this paper, we use $\Delta = 200$, larger than the virial value for our cosmology ($\Delta \sim 111$) but commonly used by other authors.

Master cluster catalogues² were produced containing only objects with at least 500 particles each of gas and dark matter, equivalent to a mass limit, $M_{\text{lim}} \approx 1.18 \times 10^{13} h^{-1} M_\odot$. At $z = 0$, the catalogues contain 428, 457 and 405 clusters for the *Non-radiative*, *Cooling* and *Preheating* simulations respectively.

For each cluster, we then estimated various observable quantities: the intrinsic SZ signal, Y^{int} , the X-ray emission-weighted gas temperature, T_X and the X-ray luminosity, L_X . We identified the hot intracluster gas as all gas particles within R_{200} with $T > 10^5$ K (in practice there are very few particles with $10^4 \text{ K} < T < 10^5$ K as their cooling times are very short) and assume full ionization, such that the number of electrons per baryon is $\eta = 0.88$ for a hydrogen mass fraction $X = 0.76$. We have

$$Y^{\text{int}} = \frac{k_B \sigma_T}{m_e c^2} \frac{\eta}{m_p} f_{\text{gas}} M T_{\text{mw}}, \quad (8)$$

where $T_{\text{mw}} = \sum m_i T_i / \sum m_i$ is the mass-weighted temperature of the gas, $f_{\text{gas}} = \sum m_i / M$ the gas fraction, m_i the mass of hot gas particle i and M the total mass of the cluster.

The X-ray emission-weighted temperature was estimated as

$$T_X = \frac{\sum_i m_i \rho_i \Lambda_{\text{soft}}(T_i, Z) T_i}{\sum_i m_i \rho_i \Lambda_{\text{soft}}(T_i, Z)}, \quad (9)$$

where ρ_i and T_i are the density and temperature of the hot gas particles. Since most observed temperatures use instruments sensitive to soft X-rays, we use a soft-band cooling function, Λ_{soft} , from Raymond & Smith (1977) for an energy range 0.3–1.5 keV.

The bolometric X-ray luminosity of each cluster, corrected from its soft-band emission, was estimated as

$$L_X = \frac{\Lambda_{\text{bol}}(T_X)}{\Lambda_{\text{soft}}(T_X)} \sum_i \frac{m_i \rho_i \Lambda_{\text{soft}}(T_i, Z)}{(\mu m_H)^2}, \quad (10)$$

where $\mu m_H = 10^{-24}$ g is the mean molecular mass of the gas and Λ_{bol} is the bolometric cooling function (Sutherland & Dopita 1993).

Finally, we imposed lower limits on T_X and L_X (by inspecting the T_X – M and L_X – M relations at all redshifts) to create (separate) catalogues that were complete in the two quantities. For example, when investigating temperature scalings at $z = 0$, all clusters with $T_X < 0.35, 0.65, 0.60$ keV (for the *Non-radiative*, *Cooling* and *Preheating* simulations respectively) were discarded, reducing the number of clusters in our catalogues by around 30 per cent in the *Cooling* and *Preheating* simulations and 46 per cent in the *Non-radiative* run. Similarly, for scalings with X-ray luminosity at $z = 0$, our original cluster catalogues were trimmed by selecting only clusters with $L_X > 2.9 \times 10^{43}, 9.0 \times 10^{41}, 4.5 \times 10^{41}$ erg s^{−1}, for the *Non-radiative*, *Cooling* and *Preheating* simulations, reducing the number of clusters in the original catalogues by about 52, 46, and 29 per cent respectively.

² The catalogues are available to download at the website virgo.sussex.ac.uk

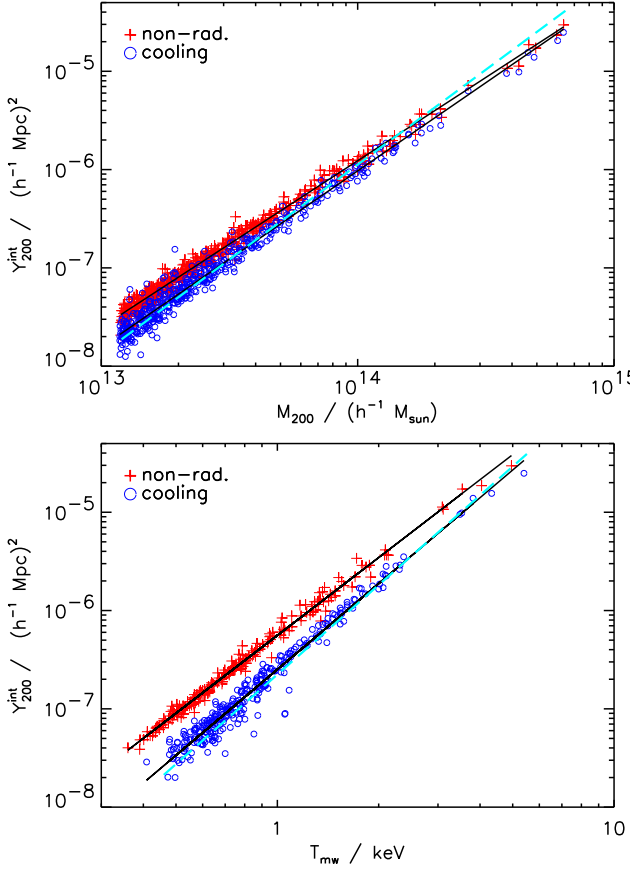


Figure 1. Scaling relations between Y_{200}^{int} & M_{200} (top panel) and Y_{200}^{int} & T_{mw} (bottom panel) for the *Non-radiative* (crosses) and *Cooling* (circles) simulations. Solid lines are power-law fits to the data from these runs, while the dashed line is the corresponding fit for clusters in the *Preheating* simulation.

4 SCALING RELATIONS AT REDSHIFT ZERO

4.1 The Y - M and Y - T_{mw} relations

We begin by correlating Y^{int} with mass and mass-weighted temperature, all measured within R_{200} . An early study of the relation between mass and SZ absorption in clusters was made in unpublished work by Metzler (1998), who verified with non-radiative simulations the related self-similar scaling, $y \propto M$. More recently, White et al. (2002) also recovered the self-similar scaling, $Y \propto M^{5/3}$, from simulations of similar size to those studied here, concluding that the combined effect of cooling and feedback (galactic winds) on the SZ properties of their clusters was small.

Fig. 1 illustrates our $Y_{200}^{\text{int}} - M_{200}$ and $Y - T_{\text{mw}}$ relations for clusters in the *Non-radiative* (crosses) and *Cooling* (circles) simulations. The solid lines represent power-law best fits to the data, while the dashed line is the best-fit to clusters in the *Preheating* simulation, omitted for the purpose of clarity. The figure shows that Y_{200}^{int} is tightly correlated with mass and mass-weighted temperature in all runs. As we shall see, however, these correlations show significantly less scatter than those relating Y with X-ray emission-weighted properties, because the latter is sensitive to substructure in the dense core gas. The best power-law fits to the $Y_{200}^{\text{int}} - M_{200}$ relation in each simulation are

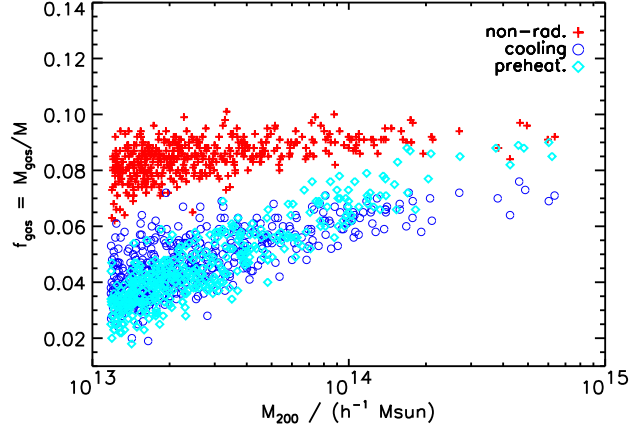


Figure 2. Fraction of hot gas within R_{200} as a function of mass for clusters in the *Non-radiative* (crosses), *Cooling* (circles) and *Preheating* (diamonds) simulations.

- *Non-radiative run:*

$$Y_{200}^{\text{int}} = 1.22 \times 10^{-6} \left(\frac{M_{200}}{10^{14} h^{-1} M_{\odot}} \right)^{1.69} (h^{-1} \text{Mpc})^2, \quad (11)$$

- *Cooling run:*

$$Y_{200}^{\text{int}} = 0.97 \times 10^{-6} \left(\frac{M_{200}}{10^{14} h^{-1} M_{\odot}} \right)^{1.79} (h^{-1} \text{Mpc})^2, \quad (12)$$

- *Preheating run:*

$$Y_{200}^{\text{int}} = 1.12 \times 10^{-6} \left(\frac{M_{200}}{10^{14} h^{-1} M_{\odot}} \right)^{1.93} (h^{-1} \text{Mpc})^2. \quad (13)$$

As expected, the slope of the fit to the *Non-radiative* clusters is close to $5/3$, the self-similar value given in Eq. (6). The slope is steeper for the *Cooling* and *Preheating* simulations however, primarily due to lower Y values for low-mass systems. This difference is due to the effects of cooling and heating on both the gas fraction and temperature of the clusters. Cooling removes low-entropy (core) gas from the halo, causing higher-entropy material to flow in to replace it. This results in a lower gas fraction although the remaining gas is hotter (Pearce et al. 2000; Bryan 2000; Muanwong et al. 2001). For low-mass clusters ($M_{200} < 10^{14} h^{-1} M_{\odot}$), the net effect of cooling on Y is dominated by the decrease in hot gas fraction, shown in Fig. 2, around a factor of two lower than the *Non-radiative* average at $M_{200} = 10^{13} h^{-1} M_{\odot}$. For the highest mass clusters this difference decreases to around 30 per cent; combined with the increase in temperature of the gas, the clusters have very similar Y values in the two simulations.

In the *Preheating* case, the energy injection at high redshift heats the gas and expels some of it from the cluster. Hence its effect on the cluster properties is similar to the cooling model but the fate of the gas is different (Muanwong et al. 2002). Fig. 2 shows that the gas fraction in *Preheating* clusters increases more rapidly with mass than for objects in the *Cooling* simulation. In low-mass systems the heating energy was sufficient to significantly decrease f_{gas} (and hence Y) but left gas fractions almost unchanged in the highest-mass clusters, where the heating resulted in only a modest net increase in temperature. Note, therefore, that the best-fit relation is only a good description of the low-mass

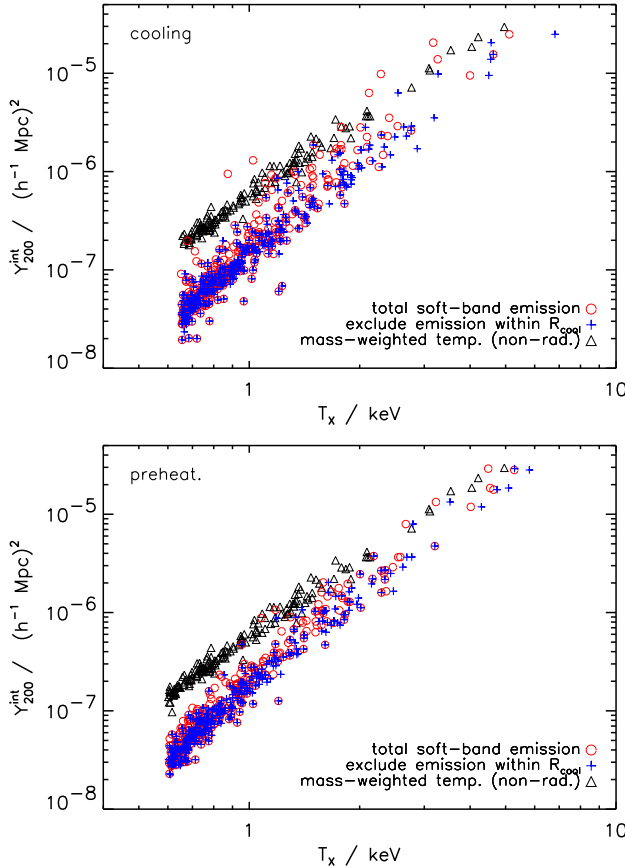


Figure 3. Y_{200}^{int} versus T_X for clusters in the *Cooling* (top panel) and *Preheating* (bottom panel) simulations, including (circles) and excluding (crosses) soft-band emission from within the cooling radius. Also shown for comparison is the scaling with the mass-weighted temperature found in the *Non-radiative* simulation (triangles).

clusters in the *Preheating* simulation; systems more massive than $\sim 10^{14} h^{-1} M_\odot$ are adequately described by the *Non-radiative* relation.

The effects of cooling and preheating on the cluster properties are more readily apparent in the relation between Y and mass-weighted temperature. For a cluster of fixed gas and total mass, $Y \propto T_{\text{mw}}$, and so heating the gas causes a shift to the right of the steeper self-similar relation ($Y \propto T^{5/2}$). Additionally, the decrease in gas fraction lowers Y , separating the two relations further. The best-fit $Y_{200}^{\text{int}} - T_{\text{mw}}$ relations are

- *Non-radiative run:*

$$Y_{200}^{\text{int}} = 5.59 \times 10^{-7} \left(\frac{k_B T_{\text{mw}}}{1 \text{ keV}} \right)^{2.63} (h^{-1} \text{ Mpc})^2 \quad (14)$$

- *Cooling run:*

$$Y_{200}^{\text{int}} = 2.51 \times 10^{-7} \left(\frac{k_B T_{\text{mw}}}{1 \text{ keV}} \right)^{2.90} (h^{-1} \text{ Mpc})^2 \quad (15)$$

- *Preheating run:*

$$Y_{200}^{\text{int}} = 2.23 \times 10^{-7} \left(\frac{k_B T_{\text{mw}}}{1 \text{ keV}} \right)^{3.03} (h^{-1} \text{ Mpc})^2. \quad (16)$$

Table 1. Power-law fits to the simulated cluster $Y - T_X$ and $Y - L_X$ scalings at $z = 0$. Here α_T and α_L are the slopes of the $Y_{200}^{\text{int}} - T_X$ and $Y_{200}^{\text{int}} - L_X$ relations, whereas $A_T/10^7$ and $A_L/10^7$ are the values of Y_{200}^{int} derived from these relations at $k_B T_X = 1 \text{ keV}$ and $L_X = 10^{43} h^{-2} \text{ erg s}^{-1}$, respectively.

Run	$Y^{\text{int}} - T_X$		$Y^{\text{int}} - L_X$	
	α_T	A_T	α_L	A_L
<i>Non-radiative</i> (bolometric)	2.47	10.1	1.26	0.37
<i>Cooling</i> (soft-band)	uncorrected	3.35	1.64	0.94
	cooling-flow corrected	3.06	1.41	1.09
<i>Preheating</i> (soft-band)	uncorrected	3.26	1.93	0.98
	cooling-flow corrected	3.18	1.70	1.04
				8.09

4.2 The $Y - T_X$ relation

Of more practical interest is to investigate how Y correlates with X-ray observables, particularly luminosity and emission-weighted temperature.

Fig. 3 illustrates the relationship between Y_{200}^{int} and T_X for the *Cooling* (top panel) and *Preheating* (bottom panel) simulations. Circles represent clusters for which all hot gas particles within R_{200} are considered, whereas crosses are for the same clusters but excluding particles within the cooling radius. We define the cooling radius as the radius within which the gas has a mean cooling time of 6 Gyr. (This procedure is an attempt to provide a ‘cooling flow’ correction to the estimated values of T_X .)

Comparing these results with Fig. 1, we see that the scatter is larger for the correlation with T_X than with T_{mw} . This is because T_X is weighted by density and temperature and is therefore more sensitive to substructure, particularly from the centres of clusters. This is also evident from the fact that the scatter is smaller when the gas within the cooling radius is excluded (note that this also increases T_X in high-mass systems, which slightly flattens the $Y - T_X$ relation).

Table 1 lists best-fit coefficients, α_T and A_T , to the power-law, $Y_{200}^{\text{int}} = (A_T/10^7) (k_B T_X/1 \text{ keV})^{\alpha_T}$ for the *Cooling* and *Preheating* runs. (We also present results from the *Non-Radiative* run, using a bolometric cooling function, and this agrees well with the self-similar scaling $Y \propto T^{5/2}$.) For a given run, the normalization of the $Y_{200}^{\text{int}} - T_X$ relation is lower and slope steeper than for the $Y_{200}^{\text{int}} - T_{\text{mw}}$ relation. The heavier weighting of the denser gas exacerbates the effects of cooling/heating on the $Y - T$ relation discussed in the previous section.

4.3 The $Y - L_X$ relation

We end this section by reporting on the $z = 0$ correlation between Y^{int} and bolometric X-ray luminosity, L_X , as inferred from the soft-band emission. Fig. 4 shows the $Y_{200}^{\text{int}} - L_X$ relation from the *Cooling* (top panel) and *Preheating* (bottom panel) simulations. Again, we use circles to represent values including all hot gas particles, whereas crosses represent results when excluding gas from within the cool-

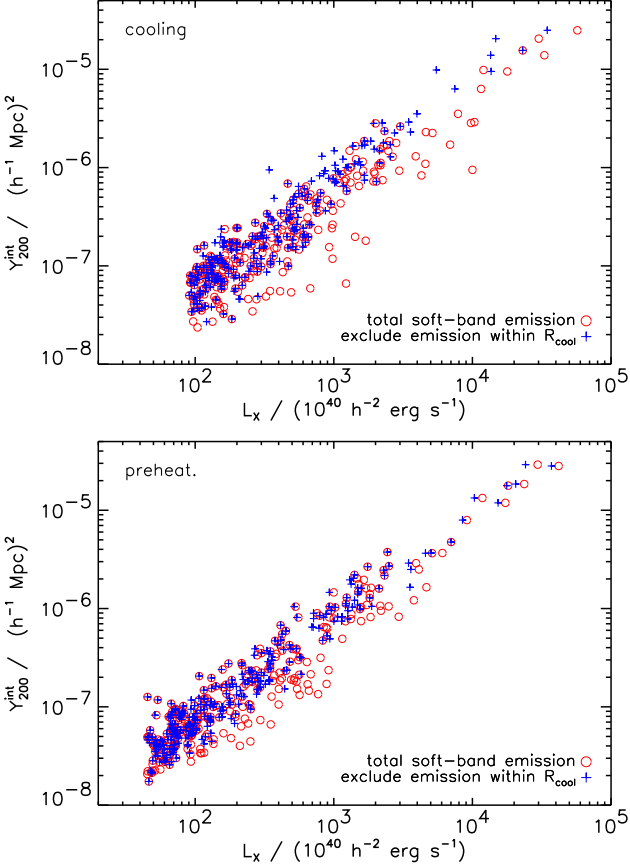


Figure 4. Y_{200}^{int} versus L_X for clusters at $z = 0$ in the *Cooling* (top panel) and *Preheating* (bottom panel) simulations. Circles (crosses) denote objects when gas within the cooling radius is included (excluded) in the calculations.

ing radius. The best-fit parameters α_L and A_L , defined by $Y_{200}^{\text{int}} = (A_L/10^7)(L_X/L_{43})^{\alpha_L}$, where $L_{43} = 10^{43}h^{-2}\text{erg s}^{-1}$, are listed in Table 1.

The *Cooling* and *Preheating* relations are significantly shallower than the predicted self-similar scaling, $Y \propto L^{5/4}$, which is well reproduced by the *Non-radiative* simulation (where $\alpha_L = 1.26$). Again, this is due to the increase in entropy of the gas, particularly in low-mass clusters, which decreases their luminosity. Omitting gas from within the cooling radius slightly increases the slope of the $Y^{\text{int}} - L_X$ relation and also reduces the scatter.

5 EVOLUTION OF SCALING RELATIONS

We now investigate the evolution of the scaling relations with redshift. In each of the following subsections, we factor out the dependence expected from self-similar evolution. Note that the self-similar evolution has no dependence on Ω_0 because we define the overdensity with respect to the comoving critical density.

5.1 Evolution of the $Y - M$ relation

Fig. 5 shows the $Y_{200} - M_{200}$ relation for clusters in the *Cooling* simulations, for a range of redshifts between $z \sim 0$

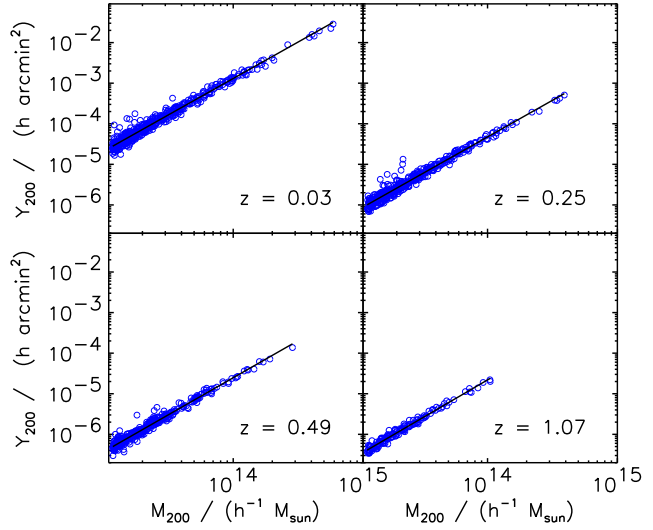


Figure 5. $Y_{200} - M_{200}$ relation at various redshifts for the *Cooling* simulation. The solid line is the power-law best fit.

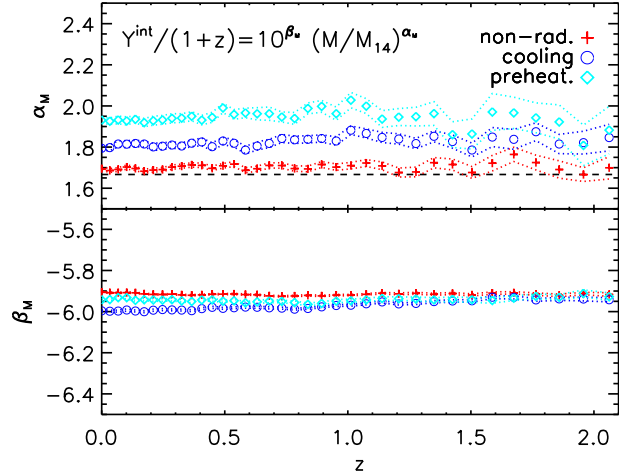


Figure 6. Redshift dependence of the slope (α_M) and normalization (β_M) of the cluster $Y_{200}^{\text{int}} - M_{200}$ relation in the *Non-radiative* (crosses), *Cooling* (circles) and *Preheating* (diamonds) simulations. Solid lines represent best-fit parameters and the dotted lines their $1-\sigma$ uncertainties (see text). The dashed line represents the slope predicted by the self-similar model ($\alpha_M = 5/3$).

and $z \sim 1$. Here we use $Y_{200} = Y_{200}^{\text{int}} d_A^{-2}$, demonstrating the dominant effect of d_A on Y at these redshifts. Note that the number of clusters satisfying our mass selection criteria, $M_{200} \gtrsim 1.18 \times 10^{13}h^{-1}\text{M}_\odot$, decreases with increasing redshift.

A noticeable feature of Fig. 5 is the apparent independence of the slope of the $Y_{200} - M_{200}$ relation with redshift. To quantify the effects of cooling and heating on the evolution of the slope, we fit a power-law

$$\frac{Y_{200}^{\text{int}}}{1+z} = 10^{\beta_M(z)} (M_{200}/10^{14}h^{-1}\text{M}_\odot)^{\alpha_M(z)}, \quad (17)$$

to the distribution of clusters at each redshift, and plot the resulting best-fit values of α_M against z in the upper panel of Fig. 6. (We do not plot results for redshifts beyond 2 as

Table 2. Deviations from self-similarity in the mean slope and normalization of the SZ scaling relations. The quantities $\langle \alpha_M \rangle$, $\langle \alpha_T \rangle$ and $\langle \alpha_L \rangle$ are the mean values of the best-fit slopes of the $Y_{200}^{\text{int}} - M_{200}$, $Y_{200}^{\text{int}} - T_X$ and $Y_{200}^{\text{int}} - L_X$ relations respectively, averaged over redshifts $z = 0$ to $z = 2$. The quantities γ_M , γ_T and γ_L are power-law best fits to the normalization of the scalings, $10^{\beta(z)} \propto (1+z)^\gamma$; the first two are a good fit for the complete redshift range, but for luminosity the fit is restricted to $0 < z < 1$.

Run	Mean slope deviation from self-similarity		
	$\langle \alpha_M \rangle - 5/3$	$\langle \alpha_T \rangle - 5/2$	$\langle \alpha_L \rangle - 5/4$
<i>Cooling</i>	0.16	0.44	-0.16
<i>Preheating</i>	0.28	0.52	-0.22
Normalization deviation from self-similarity			
Run	γ_M	γ_T	γ_L
<i>Cooling</i>	0.14	0.73	1.30
<i>Preheating</i>	0.02	0.33	1.62

the number of clusters below our mass threshold becomes too small for a reliable fit to be produced.) Crosses, circles and diamonds represent best-fit values, and dotted lines denote $1-\sigma$ uncertainties (estimated using the method given by Press et al. 1992) from the *Non-radiative*, *Cooling* and *Preheating* simulations respectively. Indeed, the results are consistent with an unevolving slope for all three models out to $z = 2$.

The lower panel of Fig. 6 shows the evolution of the normalization, obtained by fitting the same power-law function as before, but with a fixed slope taken to be equal to the mean value of $\alpha_M(z)$ within the displayed range of z (values are given in Table 2). From this figure, we see that the evolution of the $Y_{200}^{\text{int}} - M_{200}$ normalization is remarkably self-similar for all runs. Fitting a power-law, $10^{\beta_M(z)} \propto (1+z)^{\gamma_M}$, to the derived normalizations (within the displayed range of z), we find that the largest deviation from self-similar evolution of the normalization is only $\gamma_M = 0.14$, for the *Cooling* simulation (Table 2).

5.2 Evolution of the $Y - T_X$ relation

Fig. 7 shows the redshift dependence of the slope and normalization of the $Y - T_X$ relation for the *Cooling* and *Preheating* simulations, using cooling-flow corrected temperatures. As in the previous section, we first fit the cluster distribution at each redshift with a power-law

$$\frac{Y_{200}^{\text{int}}}{(1+z)^{-3/2}} = 10^{\beta_T(z)} (T_X/\text{keV})^{\alpha_T(z)}, \quad (18)$$

to determine the evolution of the slope. While this shows significant statistical oscillations (reflecting the higher sensitivity of the emission-weighted temperature to the thermal history of the gas), there is no evidence of evolution with redshift beyond that predicted by self-similarity. The slope is then fixed at the mean value, $\langle \alpha_T \rangle$, before determining the redshift dependence of the normalization, $\beta_T(z)$. Unlike the $Y^{\text{int}} - M$ relation, there is a definite evolutionary trend that is particularly significant in the *Cooling* case. Fitting the normalizations with a power-law of the form $10^{\beta_T(z)} \propto (1+z)^{\gamma_T}$, we find $\gamma_T = 0.73$ and $\gamma_T = 0.33$ for the *Cooling* and *Preheating* simulations, respectively. In both cases the normal-

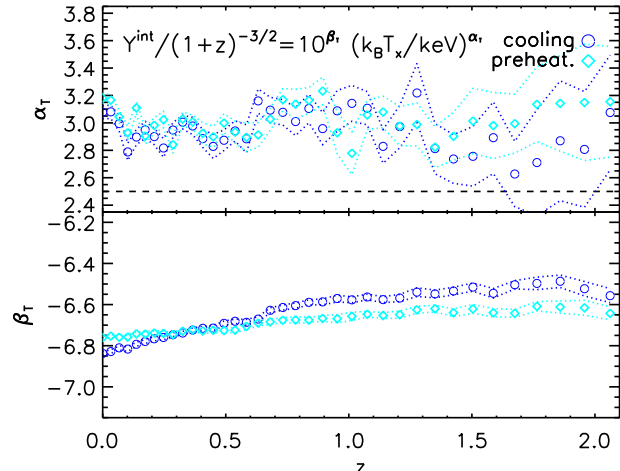


Figure 7. Redshift dependence of the slope (α_T) and normalization (β_T) of the cluster $Y_{200}^{\text{int}} - T_X$ relation in the *Cooling* (circles) and *Preheating* (diamonds) simulations. Solid lines represent best-fit values and dotted lines their $1-\sigma$ uncertainties. The dashed line represent the slope predicted by the self-similar model ($\alpha_T = 5/2$).

ization of the $T_X - M$ relation increases with time compared to the expected self-similar evolution.

5.3 Evolution of the $Y - L_X$ relation

We end by studying the evolution of the $Y - L_X$ relation, shown in Fig. 8. Our power-law fitting function was

$$\frac{Y_{200}^{\text{int}}}{(1+z)^{-27/8}} = 10^{\beta_L(z)} (L_X/L_{43})^{\alpha_L(z)}, \quad (19)$$

using cooling-flow corrected values for L_X . Again, the slopes are constant with redshift to good approximation, and there is additional evolution in the normalization. In this case a single power-law is not so good a fit over the complete redshift range, and we restrict the fit to $0 < z < 1$ which is where observations are likely to be made. Fitting a power-law $10^{\beta_L(z)} \propto (1+z)^{\gamma_L}$ yields $\gamma_L \sim 1.3$ & 1.6 in the *Cooling* and *Preheating* cases respectively (Table 2) in this redshift range, with the relation flattening at redshifts beyond one.

6 CONCLUSIONS

In this paper, we investigated the relationship between SZ and X-ray properties of clusters drawn from three simulations: a *Non-radiative* simulation, where the gas could only heat adiabatically and through shocks; a *Cooling* simulation, where the gas could also cool radiatively and a *Preheating* simulation, where we additionally heated the gas by 1.5 keV per particle at $z = 4$. We focussed on the relations between the thermal SZ signal Y_{int} and cluster mass, temperature and X-ray luminosity, both at $z = 0$ and the evolution with redshift. Our main conclusions are as follows:

- Y_{int} is tightly correlated with both mass and mass-weighted temperature. Scaling relations of Y_{int} with X-ray quantities show significantly more scatter however, due to the sensitivity of the latter (which are emission-weighted)

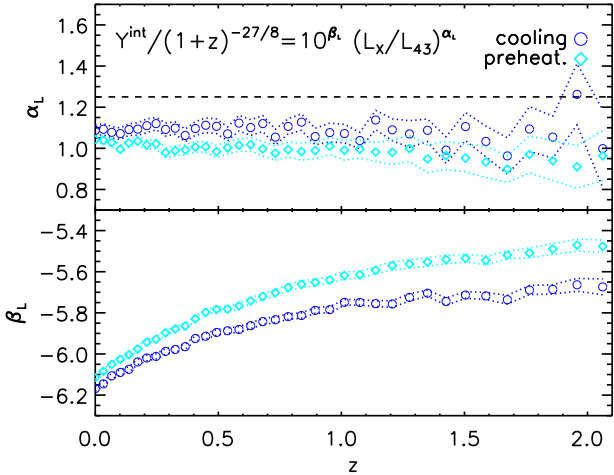


Figure 8. Redshift dependence of the slope (α_L) and normalization (β_L) of the cluster $Y_{200}^{\text{int}} - L_X$ relation in the *Cooling* (circles) and *Preheating* (diamonds) simulations. Solid lines represent best-fit parameters and dotted lines their $1-\sigma$ uncertainties. The dashed line represent the slope predicted by the self-similar model ($\alpha_L = 5/4$).

to the gas distribution in the cores of clusters. Excluding gas from within the cooling radius of each cluster reduces the scatter.

- The *Non-radiative* simulation scaling relations closely match those predicted by the self-similar model, with $Y_{\text{int}} \propto T_X^{5/2}$ and $Y_{\text{int}} \propto L_X^{5/4}$.
- *Cooling* decreases Y_{int} for a given cluster mass, due to the reduction in the hot gas fraction (which decreases Y_{int}) being more effective than the increase in temperature of the remaining gas (which increases Y_{int}). *Preheating* the gas has a similar effect except in the most massive clusters, where the heating energy was not sufficient to expel much gas from the halo. At redshift zero, the resulting $Y_{\text{int}} - T_X$ scaling relation is steeper than the self-similar relation, $Y_{\text{int}} \propto T_X^{3.0-3.4}$, and the $Y_{\text{int}} - L_X$ relation flatter, $Y_{\text{int}} \propto L_X^{0.9-1.1}$.
- There is no evidence of evolution in the slopes of any of the scaling relations. The normalization of the $Y_{200} - M_{200}$ relation is also consistent with self-similar evolution. However, the relations between Y_{int} and the cluster X-ray properties do show significant evolution in normalization relative to that expected from self-similarity, indicating that evolution is predominantly in the X-ray properties rather than the SZ properties. The effects of excess entropy reduces the negative evolution of the $Y_{\text{int}} - T_X$ and $Y_{\text{int}} - L_X$ with redshift, particularly at $z < 1$.

ACKNOWLEDGMENTS

A.C.S. was supported by the EU CMBNET network, S.T.K. by PPARC, and A.R.L. in part by the Leverhulme Trust. The simulations used in this paper were carried out on the Cray-T3E (RIP) at the EPCC as part of the Virgo Consortium programme of investigations into the formation of structure in the Universe. A.C.S. acknowledges the use of the computer facilities at CALMIP-CICT, France.

REFERENCES

Bower R. G., 1997, MNRAS, 288, 355
 Bower R. G., Benson A. J., Lacey C. G., Baugh C. M., Cole S., Frenk C. S., 2001, MNRAS, 325, 497
 Bryan G. L., 2000, ApJ, 544, L1
 Cavaliere A., Menci N., 2001, MNRAS, 327, 488
 Cole S. et al., 2001, MNRAS, 326, 255
 Couchman H. M. P., Thomas P. A., Pearce F. R., 1995, ApJ, 452, 797
 da Silva A. C., Kay S. T., Liddle A. R., Thomas P. A., Pearce, F. R., Barbosa D., 2001, ApJ, 561, L15
 Edge A. C., Stewart G. C., 1991, MNRAS, 252, 414
 Eke V. R., Navarro J. F., Frenk C. S., 1998, ApJ, 503, 569
 Evrard A. E., Henry J. P., 1991, ApJ, 383, 95
 Holder G. P., Carlstrom J. E., 2001, ApJ, 588, 515
 Kaiser N., 1986, MNRAS, 222, 323
 Kaiser N., 1991, ApJ, 383, 104
 Knight P. A., Ponman T. J., 1997, MNRAS, 289, 955
 Mather J. C., Fixsen, D. J., Shafer R. A., Mosier C., Wilkinson D. T., 1999, ApJ, 512, 511
 McCarthy I. G., Babul A., Holder G. P., Balogh, M. L., 2003a, ApJ, 591, 515
 McCarthy I. G., Holder G. P., Babul A., Balogh, M. L., 2003b, ApJ, 591, 526
 Metzler C. A., 1998, astro-ph/9812295
 Muanwong O., Thomas P. A., Kay S. T., Pearce F. R., Couchman H. M. P., 2001, MNRAS, 552, L27
 Muanwong O., Thomas P. A., Kay S. T., Pearce F. R., 2002, MNRAS, 336, 527
 Navarro J. F., Frenk C. S., White S. D. M., 1995, MNRAS, 275, 720
 Navarro J. F., Frenk C. S., White S. D. M., 1997, ApJ, 490, 493
 Pearce F. R., Couchman H. M. P., 1997, New Astronomy, 2, 411
 Pearce F. R., Thomas P. A., Couchman H. M. P., Edge A. C., 2000, MNRAS, 317, 1029
 Ponman T. J., Sanderson A. J. R., Finoguenov A., 2003, MNRAS, 343, 331
 Press W. H., Teukolsky S. A., Vetterling W. T., Flannery B. P., 1992, *Numerical Recipes in Fortran*, CUP
 Quilis V., Bower R. G., Balogh M. L., 2001, MNRAS, 328, 1091
 Raymond J. C., Smith B. W., 1977, ApJS, 35, 419
 Springel V., White M., Hernquist L., 2001, ApJ, 549, 681
 Sunyaev R. A., Zel'dovich Ya. B., 1972, Comm. Astrophys. Space Phys., 4, 173
 Sunyaev R. A., Zel'dovich Ya. B., 1980, ARA&A, 18, 537
 Sutherland R. S., Dopita M. A., 1993, ApJS, 88, 253
 Thacker R. J., Couchman H. M. P., 2000, ApJ, 545, 728
 Thomas P. A., Couchman H. M. P., 1992, MNRAS, 257, 11
 Thomas P. A., Muanwong O., Kay S. T., Liddle, A. R., 2002, MNRAS, 330, L48
 Voit G. M., Bryan G. L., Balogh M. L., Bower R. G., 2002, ApJ, 576, 601
 White M., Hernquist L., Springel V., 2002, ApJ, 579, 16
 Wu K. K. S., Fabian A. C., Nulsen P. E. J., 2000, MNRAS, 318, 889
 Xue Y.-J., Wu X.-P., 2000, ApJ, 538, 65
 Zhang Y.-Y., Wu X.-P., 2003, ApJ, 583, 529